A family of models of partially relaxed stellar systems

II. Comparison with the products of collisionless collapse

M. Trenti[1], G. Bertin[2], and T. S. van Albada[3]

[1] Scuola Normale Superiore, Piazza dei Cavalieri 7, 56126 Pisa, Italy
    e-mail: m.trenti@sns.it
[2] Dipartimento di Fisica, Università di Milano, via Celoria 16, 20133 Milano, Italy
    e-mail: Giuseppe.Bertin@unimi.it
[3] Kapteyn Astronomical Institute, Postbus 800, 9700 AV Groningen, The Netherlands
    e-mail: albada@astro.rug.nl

Abstract. *N*-body simulations of collisionless collapse have offered important clues for the construction of realistic stellar dynamical models of elliptical galaxies. Understanding this idealized and relatively simple process, by which stellar systems can reach partially relaxed equilibrium configurations (characterized by isotropic central regions and radially anisotropic envelopes), is a prerequisite to more ambitious attempts at constructing physically justified models of elliptical galaxies in which the problem of galaxy formation is set in the generally accepted cosmological context of hierarchical clustering.

In a previous paper we have discussed the dynamical properties of a family of models of partially relaxed stellar systems (the $f^{(\nu)}$ models), designed to incorporate the qualitative properties of the products of collisionless collapse at small and at large radii. Here we revisit the problem of incomplete violent relaxation, by making a direct comparison between the detailed properties of such family of models and those of the products of collisionless collapse found in *N*-body simulations that we have run for the purpose. Surprisingly, the models thus identified are able to match the simulated density distributions over nine orders of magnitude and also to provide an excellent fit to the anisotropy profiles and a good representation of the overall structure in phase space. The end-products of the simulations and the best-fitting models turn out to be characterized by a level of pressure anisotropy close to the threshold for the onset of the radial-orbit instability. The conservation of Q, a third quantity that is argued to be approximately conserved in addition to total energy and total number of particles as a basis for the construction of the $f^{(\nu)}$ family, is discussed and tested numerically.

Key words. stellar dynamics – galaxies: evolution – galaxies: formation – galaxies: kinematics and dynamics – galaxies: structure

1. Introduction

The collapse of a dynamically cold cloud of stars can lead to the formation of realistic stellar systems, with projected density profiles well represented by the $R^{1/4}$ law (van Albada 1982). The theoretical framework for the mechanism of incomplete violent relaxation that governs this process of structure formation was proposed by Lynden-Bell (1967), who argued that fast fluctuations of the potential during collapse would lead to the formation of a well-relaxed isotropic core, embedded in a radially anisotropic, partially relaxed halo. This general picture served as a physical justification for the construction of the so-called f_∞ models, which indeed recovered the $R^{1/4}$ law and, suitably extended to the case of two-component systems (to account for the coexistence of luminous and dark matter), led to a number of interesting applications to the observations (see Bertin & Stiavelli 1984, 1993, and references therein).

An attempt at deriving the relevant distribution function directly from the statistical mechanics of incomplete violent relaxation suggested that, in addition to the f_∞ models, one could consider alternative models, called the $f^{(\nu)}$ models (Stiavelli & Bertin 1987), with similar overall characteristics. The key ingredient for the construction of the $f^{(\nu)}$ distribution function is the conjecture that a *third* quantity Q, in addition to the total mass M and the total energy $E_{\rm tot}$, is *approximately* conserved during the process of collisionless collapse (of course, we are referring to systems characterized by vanishing total angular momentum, $J_{\rm tot} = 0$). This quantity is introduced to model the process of *incomplete* violent relaxation, ensuring a radially biased pressure tensor and a $1/r^4$ density profile in the outer parts of the system. Because of their relatively straightforward derivation from the Boltzmann entropy, these models were revisited recently (Bertin & Trenti 2003) and used to demonstrate the onset of the gravothermal catastrophe

(Lynden-Bell & Wood 1968) for such a one-parameter sequence (at fixed ν) of anisotropic equilibria; a preliminary inspection of the general characteristics of the $f^{(\nu)}$ models then convinced us that, with significant advantage over the f_∞ models, they might also serve as a good framework to interpret the results of simulations of collisionless collapse not only qualitatively, but also in *quantitative detail*. Therefore, we proceeded to examine their intrinsic properties systematically (Trenti & Bertin 2005, hereafter Paper I), and we will take advantage of that work for the study presented in this paper.

In this article we describe the results of a relatively wide set of numerical simulations of collisionless collapse, aimed at studying the phase space evolution and settling of the system during violent relaxation, and we then compare in detail the properties of the quasi-equilibrium end-products thus obtained with those of the $f^{(\nu)}$ models. In particular, we discuss the role played by the initial conditions and find that a certain degree of clumpiness is required for an efficient mixing in the single-particle angular momentum distribution; this form of relaxation turns out to be crucial for a good match with the $f^{(\nu)}$ family of models. The Q conservation is then studied directly by looking at its time evolution. For a significant range of collapse factors, as determined by the initial values of the virial ratio $u = (2K/|W|)_{t=0}$, an approximate conservation is indeed observed. The end-products (and thus the best-fitting models) tend to be characterized by a value of the global anisotropy parameter close to marginal stability with respect to the radial orbit instability (Polyachenko & Shukhman 1981).

The paper is organized as follows. After introducing our basic models and notation (Sect. 2), in Sect. 3 we start by reviewing the choice of the numerical code and we then check the results obtained in some test runs against the tree code of Dehnen (2000). In Sect. 4 we discuss the initial conditions adopted for the simulations of collisionless collapse, with special attention to the issue of clumpiness in phase space. In Sect. 5 we characterize the end-products of the simulations in terms of a few key indicators (i.e., central concentration, global anisotropy, density and anisotropy profiles, deviations from spherical symmetry) and describe their dependence on the initial conditions. In Sect. 6 we examine the hypothesis of the approximate conservation of Q. We then move, in Sect. 7, to the comparison of the end-products of the simulations with the $f^{(\nu)}$ models (in terms of density and anisotropy profiles and directly in phase space). In Sect. 8, we draw the main conclusions from this study. Finally, in the Appendix we provide additional comments on the issue of clumpiness in phase space.

2. $f^{(\nu)}$ models, units, and notation

In general, we will keep the same notation as in Paper I. We recall that the relevant distribution function is obtained by extremizing the Boltzmann entropy $S = -\int f \log f \mathrm{d}^3 x \mathrm{d}^3 w$ at fixed total mass $M = \int f \mathrm{d}^3 x \mathrm{d}^3 w$, total energy $E_{\mathrm{tot}} = 1/3 \int E \mathrm{d}^3 x \mathrm{d}^3 w$, and $Q = \int J^\nu |E|^{-3\nu/4} f \mathrm{d}^3 x \mathrm{d}^3 w$. Here E and J denote single-star specific energy and angular momentum, while x and w denote positions and velocities respectively. This leads to the function $f^{(\nu)} = A \exp\left[-aE - d(J^2/|E|^{3/2})^{\nu/2}\right]$, where a, A, d, and ν are positive constants. The $f^{(\nu)}$ models are

then constructed by solving the Poisson equation for the unknown potential $\Phi(r)$ numerically. At a fixed value of ν, one may think of the free constants as providing two dimensional scales (for example, M and E_{tot}) and one dimensionless parameter, such as $\Psi \equiv -a\Phi(0)$, the central depth of the dimensionless potential well. By $(1; 5)$ $f^{(\nu)}$ model we will denote the model of the $f^{(\nu)}$ family with $\nu = 1$ and $\Psi = 5$.

The $f^{(\nu)}$ models represent equilibrium configurations designed to describe the products of incomplete violent relaxation. They are characterized by a density profile $\rho(r)$ falling off as $1/r^4$ at large radii and as $1/r^2$ in the inner part of the system, outside a central "core". The size of the core becomes smaller as the concentration parameter Ψ increases. On the large scale, apart from such freedom in central concentration and core size, the shape of the density profile is basically independent of the $(\nu; \Psi)$ parameters (see Fig. 3 in Paper I). Interestingly, although this feature had not been imposed at the beginning (when the function $f^{(\nu)}$ is constructed), the projected density distribution of the $f^{(\nu)}$ models is typically well fitted, on the large scale, by the $R^{1/4}$ law; residuals in the fit are reduced if one considers the generalized $R^{1/n}$ law (with n a free parameter; Sersic 1968), depending on Ψ (see Figs. 4–5 in Paper I).

In contrast with other approaches (e.g., see Osipkov 1979; and Merritt 1985) where the anisotropy profile is assigned a priori, in the $f^{(\nu)}$ models the velocity dispersion anisotropy profile $\alpha(r)$, defined as $\alpha(r) = 2 - (\langle w_\theta^2 \rangle + \langle w_\phi^2 \rangle)/\langle w_r^2 \rangle$, must be computed a posteriori and its shape depends on ν and Ψ (see Fig. 6 in Paper I). The structure of the distribution function only guarantees that the models match the asymptotic requirements suggested by the picture of incomplete violent relaxation, i.e. at large radii, where the pressure is radial, and in the central regions, where the pressure is isotropic. The global anisotropy, measured by the quantity $2K_{\mathrm{r}}/K_{\mathrm{T}}$, i.e. twice the ratio of the radial to the tangential kinetic energy, depends on the choice of $(\nu; \Psi)$ and correlates with the central concentration (e.g., see Fig. 7 in Paper I). Models with $\Psi \lesssim 4$ are characterized by an excessive degree of radial anisotropy (i.e. $2K_{\mathrm{r}}/K_{\mathrm{T}} \gtrsim 1.7$), and are thus unstable.

The physical system of units adopted in this paper is defined by 10 kpc for length, $10^{11} M_\odot$ for mass, and 10^8 yr for time. In this system, natural for studies on galactic scales, velocities are measured in units of ≈ 97.8 km s^{-1} and the value of the gravitational constant G is 4.4971.

The majority of simulations consists of runs starting from 20 cold clumps of 16 kpc radius in a sphere of 40 kpc radius, with $u = (2K/|W|)_{t=0}$ in the range 0.05–0.25. After the collapse the system has a half-mass radius around 8 kpc. The total mass of the system is $2 \times 10^{11} M_\odot$. The dynamical time, which we define as $t_{\mathrm{d}} = GM^{5/2}/(-2E_{\mathrm{tot}})^{3/2}$, is therefore typically $\approx 1.2 \times 10^8$ yr, i.e. 1.2 in our units. As a result, when we stop the simulation at time 80, the system has evolved for several tens of dynamical times. In any case, we should recall that the results obtained are scale-free, that is they can be rescaled to other choices of mass and radius if so desired.

3. The code

Direct *N*-body simulations of self-gravitating stellar systems require huge amounts of computing time because of the N^2 scaling of the code complexity with the number of particles employed. To model the evolution of collisionless systems, several algorithms have been developed that treat the gravitational interactions approximately, with a lower complexity. In principle, to study the process of collisionless collapse we have two options: either a tree code (e.g., Barnes & Hut 1986) or a particle-mesh like algorithm (e.g., see van Albada 1982; McGlynn 1984; Hernquist & Ostriker 1992). Tree codes are intrinsically slower, scaling as $N \log N$, with respect to particle-mesh Poisson solvers, for which the complexity is linear in N, but the latter have the disadvantage of a lower spatial resolution, being limited by the size of the grid used.

In this paper we are interested in the large scale structure of the end-products of collisionless collapse, for systems that do not exhibit large deviations from spherical symmetry. The natural choice thus appears to be that of a particle-mesh code, based on a spherical grid and an expansion in spherical harmonics.

The code used in the present study is thus a new version of the van Albada (1982) code. The relevant changes introduced are briefly described below, in Sect. 3.1. For completeness, we have also run (see Sect. 3.2) a number of comparison simulations with the fast code developed by Dehnen (2000).

3.1. An improved particle-mesh code

The key feature of the van Albada (1982) code is the solution of the Poisson equation $\nabla^2 \Phi = 4\pi G \rho$, which relates the mean potential Φ of the system to the mass density ρ, by means of Fourier techniques. Once the potential has been computed by expanding the density in spherical harmonics, the acceleration is obtained by numerical differentiation, and the particles are advanced by a fixed time step, using a leap-frog scheme.

At variance with the original implementation, to preserve accuracy and to avoid systematic errors, we decided to drop the angular grid and to treat the angular dependence of the force exactly, in terms of the single-particle Legendre polynomials (for further details, see Trenti 2005). Basically, this choice changes the code in the direction of the code of McGlynn (1984) and of the self-consistent field code of Hernquist & Ostriker (1992). We preferred to keep the radial grid because of its flexibility with respect to the density profile, especially under conditions of rapid evolution (we use a subroutine to generate a grid containing a fixed fraction of the total mass in each shell).

The density is assigned to the radial grid by means of a cloud-in-cell scheme with a linear kernel, i.e. a particle contributes to the density of the two closest cells with a weight depending linearly on the distance from the center of the cell considered. The same kernel is then used to assign the force from the grid to the particle. The time step is adaptively chosen in such a way that particles are not allowed to cross more than one radial cell during one step.

The code has been tested extensively, in terms of its accuracy in conserving total energy and total angular momentum for equilibrium and non-equilibrium initial conditions and in
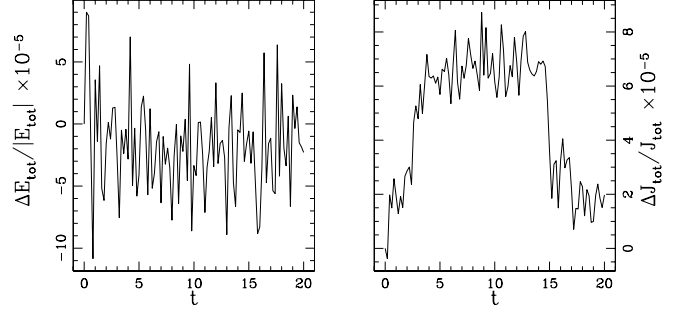

Fig. 1. Total energy conservation (*left*) and angular momentum (*right*) for a simulated $(1; 5)$ $f^{(\nu)}$ equilibrium model with 4×10^5 particles. The mass of the system is $M = 1$, the total energy $E_{\text{tot}} = -1.73$, and the half-mass radius $r_{\text{M}} = 0.5$. The magnitude of the total angular momentum associated with the initial conditions corresponds to a value of the dimensionless rotation parameter $\lambda = J_{\text{tot}}|E_{\text{tot}}|^{1/2}/(GM^{5/2}) \approx 10^{-4}$. We recall that time is given in units of 10^8 years, which, in this case, corresponds to $\approx 1.4\, t_{\text{d}}$, with $t_{\text{d}} = GM^{5/2}/(-2E_{\text{tot}})^{3/2}$.

conserving single-particle energy and angular momentum for runs of spherically symmetric equilibrium models. The modified Poisson solver scheme combined with the adaptive grid ensures a significantly better accuracy than in the original implementation. The typical total energy and total angular momentum conservation for a run with 10^5 particles is of the order of 10^{-5} per dynamical time in quasi-stationary configurations (see Fig. 1).

3.2. Comparison with Dehnen's code

As a further test, we have also run a few test simulations by comparing, under identical conditions, the performance of our code to that of the fast tree code *GyrfalcON* (Dehnen 2000, 2002), within the *NEMO* distribution (Teuben 1995). In such tests, we adopt the following procedure. We first generate the initial conditions in the physical units used by our code (see Sect. 2) and we run the simulation. We then convert the initial conditions to the natural units defined by Heggie & Mathieu (1986) and used in Dehnen's code. Finally, we run the simulation within the *NEMO* environment. The quality of the integration is checked with the standard *NEMO* tools of analysis. At the end of the simulation, a "snapshot" of the system is exported and converted back to our units, in such a way that it can be processed by the same diagnostics used for the particle-mesh code.

The initial conditions for these runs have been chosen in order to be representative of the sample investigated in this paper; they are described in Table 1 ($C4.1$ and $C4.3$ entries), with the properties of the final equilibrium state listed in Table 2.

For the runs with Dehnen's tree code we adopted the following choice of integration parameters: tolerance parameter $\theta = 0.5$ (standard choice 0.6) to improve accuracy in the calculation of forces; softening length $\epsilon = 0.01$ (in natural units; standard choice 0.05) to increase central resolution; minimum allowed time step $1/2^8$ (i.e. ≈ 724 steps per dynamical time). With this choice of integration parameters, the energy and angular momentum conservation is very good: in one

Table 1. Initial conditions for the simulations. After the simulation identifier the columns list the number of particles N, the number of clumps N_C, the initial virial ratio u, the initial values of the shape parameters ϵ_0 and η_0, and the initial concentration $C_{\rho 0}$. For the exact definitions and for the general characteristics of the groups ($C1$ to $C4$, U and S), see description in Sect. 4.2. Four simulations, marked by a $*$, have been carried out with *GyrFalcOn* (Dehnen 2000); two of them ($C4.1^*$ and $C4.3^*$) start from the same initial conditions as for $C4.1$ and $C4.3$ respectively, while $C4.4^*$ and $CP5.2^*$ are characterized by small clumps (with radius 2.8 kpc and 6 kpc respectively, distributed in a sphere of radius 40 kpc).

	N	N_C	u	ϵ_0	η_0	$C_{\rho 0}$
$C1.1$	10^5	10	0.275	0.83	0.70	3.0
$C1.2$	10^5	10	0.25	0.83	0.70	3.0
$C1.3$	10^5	10	0.225	0.83	0.70	3.0
$C1.4$	10^5	10	0.20	0.83	0.70	3.0
$C1.5$	10^5	10	0.175	0.83	0.70	3.0
$C1.6$	10^5	10	0.15	0.83	0.70	3.0
$C1.7$	10^5	10	0.125	0.83	0.70	3.0
$C1.8$	10^5	10	0.1	0.83	0.70	3.0
$C1.9$	10^5	10	0.075	0.83	0.70	3.0
$C1.10$	10^5	10	0.05	0.83	0.70	3.0
$C2.1$	8×10^5	20	0.23	0.93	0.73	2.8
$C2.2$	8×10^5	20	0.17	0.93	0.73	2.8
$C2.3$	8×10^5	20	0.12	0.93	0.73	2.8
$C2.4$	8×10^5	20	0.06	0.93	0.73	2.8
$C3.1$	8×10^5	20	0.08	0.95	0.91	2.2
$C3.2$	8×10^5	20	0.18	0.86	0.80	2.6
$C3.3$	8×10^5	20	0.15	0.84	0.70	3.1
$C3.4$	8×10^5	20	0.23	0.88	0.73	2.0
$C3.5$	8×10^5	20	0.15	0.95	0.88	3.7
$C3.6$	8×10^5	10	0.15	0.86	0.80	3.7
$C4.1$	10^5	10	0.15	0.87	0.80	2.8
$C4.1^*$	10^5	10	0.15	0.87	0.80	2.8
$C4.1_h$	10^5	10	0.15	0.87	0.80	2.8
$C4.2$	10^5	20	0.25	0.75	0.63	1.5
$C4.3$	10^5	80	0.14	0.90	0.77	1.9
$C4.3^*$	10^5	80	0.14	0.90	0.77	1.9
$C4.4^*$	10^5	80^+	0.15	0.85	0.78	2.0
$C4.5$	10^5	400	0.23	0.99	0.95	0.8
$C4.5_h$	10^5	400	0.23	0.99	0.95	0.8
$CV5.1$	10^5	10	0.23	1.00	1.00	1.0
$CP5.2^*$	10^5	40	0.15	0.81	0.78	0.7
$U6.1$	8×10^5	N/A	0.10	1.00	1.00	1.0
$U6.2$	8×10^5	N/A	0.19	1.00	1.00	1.0
$U6.3$	8×10^5	N/A	0.29	1.00	1.00	1.0
$U6.4$	8×10^5	N/A	0.39	1.00	1.00	1.0
$S4.2$	10^5	N/A	0.25	1.00	0.99	1.5
$S4.3$	10^5	N/A	0.15	1.00	1.00	1.9

Table 2. Final configurations for the simulations of collisionless collapse listed in Table 1. The column entries are described in Sect. 5. Note that the anisotropy profile in homogeneous simulations can be non-monotonic; this is indicated by $\dagger$. All simulations of type $C1$ and $C2$ start from identical initial conditions within each series, except for a constant scaling of velocities. The quantity ΔQ is referred to $\nu = 5/8$ in simulation $CV5.1$, to $\nu = 1$ in simulation $U6.1$ and to $\nu = 3/4$ in simulation $U6.2$; this is indicated by $\#$.

	ΔM	ΔQ	C_ρ	κ	r_α/r_M	ϵ	η
$C1.1$	0.00	0.13	570	1.61	1.02	0.91	0.73
$C1.2$	0.002	0.17	600	1.60	0.94	0.91	0.74
$C1.3$	0.01	0.20	680	1.59	0.94	0.90	0.76
$C1.4$	0.01	0.24	790	1.57	0.88	0.95	0.79
$C1.5$	0.02	0.30	720	1.52	0.88	0.96	0.81
$C1.6$	0.03	0.38	820	1.50	0.93	0.99	0.80
$C1.7$	0.04	0.44	760	1.47	0.92	0.97	0.78
$C1.8$	0.05	0.52	850	1.53	0.87	0.96	0.79
$C1.9$	0.06	0.66	1130	1.67	0.75	0.97	0.75
$C1.10$	0.08	0.72	1090	1.74	0.79	0.94	0.69
$C2.1$	0.01	0.13	110	1.52	1.49	0.87	0.78
$C2.2$	0.02	0.25	160	1.62	1.24	0.88	0.78
$C2.3$	0.03	0.4	270	1.70	0.83	0.81	0.69
$C2.4$	0.07	0.5	520	1.76	0.74	0.81	0.63
$C3.1$	0.003	0.47	1690	1.99	0.44	0.90	0.73
$C3.2$	0.001	0.26	1250	1.85	0.55	0.93	0.70
$C3.3$	0.04	0.57	430	1.60	1.34	0.92	0.71
$C3.4$	0.02	0.23	500	1.65	1.15	0.93	0.81
$C3.5$	0.005	0.24	950	1.73	0.57	0.96	0.72
$C3.6$	0.005	0.27	690	1.79	0.75	0.80	0.77
$C4.1$	0.005	0.27	440	1.77	0.83	0.80	0.73
$C4.1^*$	0.01	0.27	360	1.68	0.97	0.89	0.74
$C4.1_h$	0.00	0.18	240	1.86	0.51	0.86	0.83
$C4.2$	0.12	0.10	160	1.40	1.65	0.90	0.78
$C4.3$	0.10	<0.01	70	1.60	1.53	0.84	0.74
$C4.3^*$	0.07	0.15	70	1.50	1.56	0.86	077
$C4.4^*$	0.04	0.4	4000	1.15	5.30	0.98	0.96
$C4.5$	0.125	0.02	20	1.20	1.74	0.96	0.95
$C4.5_h$	0.10	0.05	15	1.16	1.58	0.99	0.97
$CV5.1$	0.12	$0.02^\#$	90	1.55	1.50	0.91	0.75
$CP5.2^*$	0.10	0.01	590	1.33	2.20	0.83	0.76
$U6.1$	0.33	$0.29^\#$	8	1.10	$1.60^\dagger$	1.00	1.00
$U6.2$	0.20	$0.01^\#$	6	1.10	$1.56^\dagger$	1.00	1.00
$U6.3$	0.06	0.14	9	1.11	$1.50^\dagger$	1.00	1.00
$U6.4$	0.00	0.09	8	1.11	$1.60^\dagger$	1.00	1.00
$S4.2$	0.00	0.09	506	2.13	0.29	0.99	0.98
$S4.3$	0.10	0.26	50	1.50	0.97	0.98	0.98

dynamical time t_d, the relative changes are $\Delta E_{tot}/E_{tot} < 10^{-5}$ and $\Delta J_{tot}/J_{tot} < 10^{-4}$.

The required CPU time to complete the simulation is marginally higher than with our code, which, however, has not yet been optimized for speed.

As desired, for these runs we find a substantial similarity in the properties of the end-products obtained by the two different methods of integration (see Fig. 2). To be sure, small differences naturally arise, as expected. The main systematic difference is in the degree of anisotropy characterizing the end-products of the simulations. In fact, the output from the tree code is slightly more isotropic: the final global anisotropy, measured by $2K_r/K_T$, is up to 7% lower, with a slight outward shift of the anisotropy profile, corresponding to a more efficient core relaxation. This might be related to the residual collisionality present in the tree code.
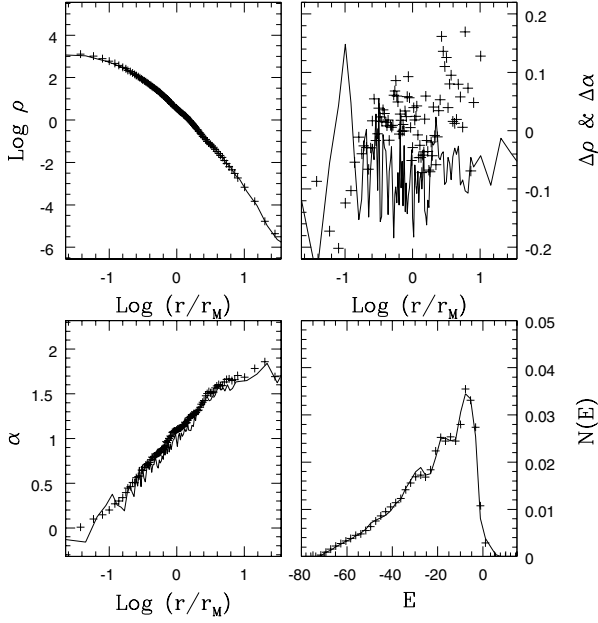
Fig. 2. Comparison between our code and *GyrFalcON* (Dehnen 2000) for the run $C4.1$. Final density (upper left) and anisotropy (bottom left) profiles, and single-particle energy distribution (bottom right) for a run starting from 10^5 particles in 10 cold clumps with $u = 0.15$ (see Tables 1 and 2 for further details about the simulation; here the solid lines give the results obtained with *GyrFalcON*, while the crosses refer to our code. In the upper right panel we plot the differences in the density profile $\Delta\rho = 2(\rho_{\rm falcon} - \rho_{\rm pm})/(\rho_{\rm falcon} + \rho_{\rm pm})$ (crosses) and in the anisotropy profile $\Delta\alpha = \alpha_{\rm falcon} - \alpha_{\rm pm}$ (solid line).

4. Choice of initial conditions

If the initial conditions are not too artificial, during the process of collisionless collapse violent relaxation can take place, with significant mixing in phase space, and wipe out much of the details that characterize the initial conditions. In reality, violent relaxation is incomplete. Therefore, the final state is that of an approximate dynamical equilibrium characterized by an anisotropic distribution function, different from a Maxwellian (which would correspond to thermodynamic equilibrium). Because of such incomplete relaxation, the end-products of the simulations do conserve some memory of the initial state.

4.1. Uniform initial conditions, clumpy initial conditions, and the cosmological framework

Some of the papers addressing the problem of collisionless collapse start from "uniform" initial conditions in position and velocity space. For example, Aguilar & Merritt (1990) assume an initial $1/r$ density profile and then explore the way the collapse proceeds by varying, in addition to the initial virial ratio $u = (2K/|W|)_{t=0}$, the shape of the initial density profile (by shrinking the system along one axis) and the amount of rotation. Udry (1993) starts from uniform cold spheres, and also varies, in addition to the above-mentioned parameters, the

initial anisotropy content $2K_{\rm r}/K_{\rm T}$. Recently, Boily et al. (2002), starting from cold uniform spheres or spheroids, focus on the effects introduced by the number of particles used in the simulation.

A few earlier investigations (van Albada 1982; McGlynn 1984; May & van Albada 1984; Londrillo et al. 1991) compared "clumpy" to "uniform" (or "homogeneous") initial conditions, showing that clumpy initial conditions lead to end-states with projected density distributions well fitted by the $R^{1/4}$ law (although Aguilar & Merritt 1990 point out that, for very small values of u, the $R^{1/4}$ law is approximately recovered even for homogeneous initial conditions). (Udry (1993) argues that starting from a multi-component initial mass spectrum for the simulation particle distribution can be an alternative way to represent a clumpy initial density configuration. However, the introduction of simulation particles so massive as to be representative of clumps would introduce effects of dynamical friction that per se would go beyond the picture of collisionless violent relaxation.)

Recently Roy & Perez (2004) studied the outcome of violent collapse starting from an initial uniform background with the possible addition of small clumps of stars. Although their clumpy initial conditions are rather different from those considered in the present paper, they also noted that clumpy simulations lead to steep density profiles with small cores.

As will also be demonstrated later on (see Sect. 5.3), the key point that distinguishes clumpy from uniform initial conditions is that, in general, only the former allow significant mixing in phase space, thus making it possible for violent relaxation to proceed properly. Thus in this paper we will focus on simulations starting from clumpy configurations. As discussed below, for the present study we do not require that our initial clumps be in internal dynamical equilibrium, since their purpose is to avoid excessive homogeneity in the (E, J^2) phase space (see also Appendix). In particular, the clumps are *not* intended to be a realistic representation of possible conditions at a given epoch in the past. In fact, the effects of violent relaxation become important in a few dynamical times, independently of the precise epoch when the process is imagined to occur.

To be sure, to identify a realistic set of initial conditions one should consider a satisfactory cosmological framework. We plan to do this in future investigations, because this would lead us well beyond the scope of the present paper. In this respect, the use of clumps is already one important step forward with respect to the use of homogeneous initial conditions. Eventually, we should devise a method for determining a "spectrum" of clumps with properties compatible with the expectations of current cosmological scenarios (see also Katz 1991, and further discussion in the Appendix). For the moment, we are satisfied with identifying the initial conditions under which sufficient mixing in phase space is guaranteed. Note that cosmologically oriented simulations are centered on the clustering and growth of dark matter halos, while in this paper, given our focus on the $R^{1/4}$ law and on the deviations from it, we have in mind mostly luminous matter.
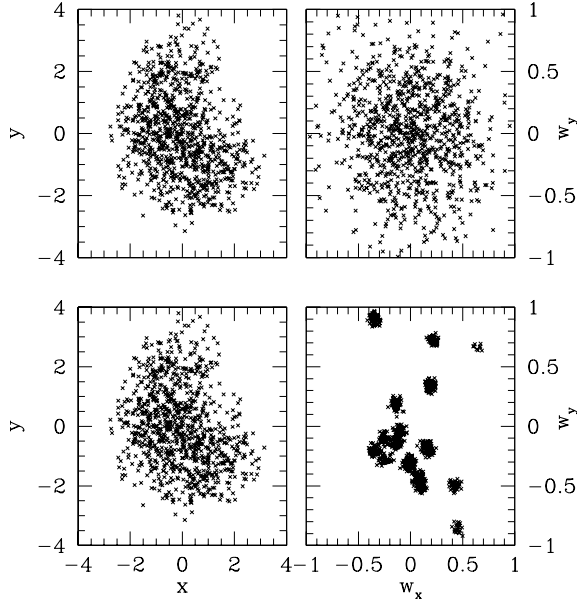
Fig. 3. Typical projected distributions in position (*left*) and velocity (*right*) space for hot (upper panels, run $C4.1_h$) and cold (lower panels, run $C4.1$) clumpy initial conditions.

4.2. Setting up clumpy initial conditions

In a clumpy initial state the N particles are grouped in N_C spherical clumps, each of them containing N_i stars, so that $N = \sum_{i=1}^{N_C} N_i$, with $\langle N_i \rangle = N/N_C$. Within each clump the star distribution is homogeneous. The centers of mass of the clumps are distributed uniformly inside a sphere of radius R, which defines the size of the system at the beginning of the simulation. The clump radius is R_C, with $R_C < R$, but such that $N_C \times R_C^3 > R^3$ (this condition ensures that the sphere of radius R is well filled by stars). The initial kinetic energy may be associated with the ordered motion of the center of mass of each clump (this is our default choice for the simulations of type C described below; in this case the velocity is assigned by drawing from an isotropic distribution) or with the random motions of the stars within the clump (in these cases we add a subscript h to the simulation label; here the center of mass of each clump is taken to be at rest). In general, with this choice of initial conditions the clumps are not in internal dynamical equilibrium. We note that when the number of clumps used is low, the initial configuration may deviate significantly from spherical symmetry (with projected shapes up to those of an $E3$ galaxy). Formally the limits $N_C \longrightarrow N$ and $N_C \longrightarrow 1$ both lead to homogeneous initial conditions.

In the case of homogeneous initial conditions (simulations of type U and S), which we run for comparison, we employed two kinds of distribution: (1) a constant density within a sphere of radius R; (2) a symmetrized version of a given clumpy configuration (simulations of type S). The symmetrization process in (2) is performed by accepting the radius and the magnitude of the velocity of each particle, following the procedure for initial clumpy conditions, but by redistributing the angular variables uniformly.

In principle, we have a wide parameter space to explore, because we have to deal with the initial virial ratio u, the number and size of the clumps, the cold/hot choice for the initial kinetic energy distribution (and the intermediate range of possibilities), the spatial distribution of the centers of mass of the clumps and of the stars within each clump. As noted earlier (e.g., see Londrillo et al. 1991), we anticipate that the main controlling physical parameter is the initial virial ratio.

Table 1 lists for each simulation the following information: the number N of particles used, the number of clumps N_C, the initial virial ratio u, the initial values of the shape parameters ϵ_0, η_0 (based on the lengths of the axes of the homogeneous ellipsoid associated with the inertia tensor, taken to be in the order $a \geq b \geq c$, so that $\eta = c/a$ and $\epsilon = b/a$; the inertia tensor is referred to the particles within a sphere of radius $3r_M$), and the initial concentration $C_{\rho 0} = (\rho(0)/\rho(r_M))_{t=0}$. As a summary for the notation used, we note the following. We have divided the set of clumpy simulations in five subsets, from $C1$ to $C5$. The simulations belonging to $C1$ start with 10^5 particles in 10 clumps, the positions of which are fixed. The $C2$ series is a high resolution (8×10^5 particles) version of $C1$, but uses instead 20 clumps. In the $C3$ (high resolution, 8×10^5 particles) and $C4$ (10^5 particles) series we use different seeds for the initial positions of the clumps and we also change other parameters as described in Table 1. Runs $CV5.1$ and $CP5.2^*$ are test runs specially performed to clarify some issues related to clumpiness (see Appendix). $CV5.1$ has clumpy conditions in velocity space as in run $C4.1$, but uniform homogeneous conditions in position space; in turn, $CP5.2^*$ has a clumpy configuration in position space (40 clumps of 6 kpc, with a filling factor $N_C \times R_C^3/R^3 = 0.135$) and uniform conditions in velocity space. Runs U refer to uniform homogeneous spheres (here the seed for the random numbers is not relevant given the high symmetry of the configuration) and the S series refers to the symmetrized runs.

5. The products of collisionless collapse

Table 2 lists for each simulation the following information: the relative mass loss for the end-products $\Delta M = (M_0 - M)/M_0$, the relative conservation of the global quantity Q, with $\Delta Q = |Q_0 - Q|/Q_0$ referred to $\nu = 1/2$ unless otherwise noted, the concentration $C_\rho = \rho(0)/\rho(r_M)$ of the end-products in terms of the ratio of the central density to the density at the half-mass radius, the global anisotropy parameter $\kappa = 2K_r/K_T$, the anisotropy radius (defined by the relation $\alpha(r_\alpha) = 1$) relative to the half-mass radius r_α/r_M, and the final shape parameters ϵ and η. All quantities are referred to the final system of bound particles.

5.1. General properties

From the results reported in Table 2 we may infer some empirical trends. In particular, here we focus on: (1) central concentration; (2) anisotropy content; (3) deviations from spherical symmetry; (4) mass loss. Density and anisotropy profiles will be discussed and compared with our theoretical models in Sect. 7.
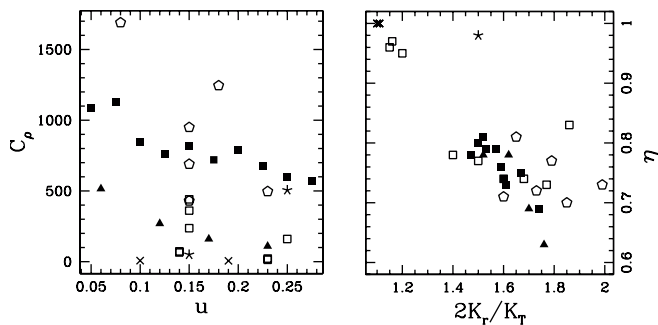
Fig. 4. Correlations between final concentration C_ρ and initial virial ratio u (*left*), and between final ellipticity η and final global anisotropy $2K_r/K_T$ (*right*). Symbols mark the various sets of simulations as follows: filled squares for $C1$, filled triangles for $C2$, open pentagons for $C3$, open squares for $C4$, crosses for U, and stars for S.

We have run two series of simulations (type $C1$ and $C2$) for which the initial particle positions and velocities are kept fixed within each series, except for a constant scaling factor in the velocities able to lead to different values of u (from 0.05 to 0.275 for $C1$ and from 0.06 to 0.24 for $C2$). This procedure thus allows us to explore the role of the initial virial ratio by keeping all other conditions strictly fixed.

The central concentration resulting from the collapse is expected to correlate with u. Londrillo et al. (1991) proposed a simple criterion to set an upper limit to the expected value of the central concentration by imposing the conservation of the maximum density in phase space. They argued that, for the collapse of an initially homogeneous system, the central concentration measured in terms of the ratio $r_M/r_{0.1}$ (of the half-mass radius to the radius of the sphere containing one tenth of the total mass) should scale as $1/u$. Our $C1$ and $C2$ simulations follow qualitatively the proposed trend. However, since relaxation is incomplete, it is natural to find that other factors, in addition to the value of u, can contribute to determine the properties of the final states. In fact, if we do not restrict our attention to the $C1$ and $C2$ sequences only and consider instead the entire set of simulations, we see that the correlation between u and C_ρ becomes weaker (see Fig. 4).

Differently from $C1$ and $C2$, the sets of $C3$ and $C4$ simulations, starting from different spatial configurations (different number and size of clumps, different seed in the random number generator), allow us to study other possible correlations, in particular those between initial and final concentration and between final concentration and initial deviations from spherical symmetry; the latter correlation was noted by Boily et al. (2002), starting from homogeneous spheroids. Again, if we include the entire set of simulations, the correlations that we find are, in general, relatively weak.

The final global anisotropy of the simulations (see the quantity κ in Table 2) is also weakly correlated with u, with larger values of u preferentially associated with lower levels of radial anisotropy. The series $C1$ has a systematic, but curiously non-monotonic trend, while $C3$ and $C4$ show that other factors, in addition to u, are important.

As to the shapes of the products of collisionless collapse, we note a relatively strong correlation (see Fig. 4) between the

final shape (as measured by η) and the final level of global anisotropy (as measured by $2K_r/K_T$). This is likely to be related to the action of the radial orbit instability during collapse. In particular, for the $C2$ series lower values of u lead to more anisotropic and more flattened end products; the effect in the $C1$ series is less pronounced. Of course, the issue of the final shapes produced by collapse has been addressed by several investigations in the past, especially with the hope of establishing whether related dynamical mechanisms can account for the observed morphologies of elliptical galaxies (for simulations in the cosmological context, see Warren et al. 1992; see also Udry 1993).

Initial conditions with a small number of clumps, as considered in our paper, often show significant deviations from spherical symmetry (from Table 1 we see that η_0 can be as low as 0.7). Curiously, the final value of η may even slightly exceed the value of η_0, thus showing that collapse may sometimes push the system toward spherical symmetry, not necessarily away from it.

Collisionless collapse can produce significant amounts of unbound particles and consequently give rise to mass loss. This effect is particularly severe in the cases where the collapse originates from a homogeneous sphere (see also Londrillo et al. 1991); here the system may lose up to one third of the mass (see run $U6.1$). Clumpiness appears to have a stabilizing effect with respect to mass loss; in fact, the mass lost is less than 7% even for run $C1.1$ characterized by $u = 0.06$. On the other hand, symmetrized clumpy initial states, of type S, are also found to evolve with limited mass loss. (Since the nature of the gravitational forces is mainly radial for both the collapsing homogeneous spheres (U simulations) and symmetrized clumpy configurations (S), the different amounts of mass loss might be related to the different radial density distributions for the two types of run. In fact, the effect of superimposing several clumps of particles creates a density profile decreasing approximately linearly with radius.)

5.2. The role of the radial orbit instability

Spherical stellar systems with an excess of radial orbits ($2K_r/K_T > 1.7 \pm 0.25$) are expected to be unstable and to evolve rapidly, on the dynamical time-scale, into ellipsoids; the precise value for the onset of the radial-orbit instability depends on the detailed structure of the system considered (Polyachenko & Shukhman 1981; see Palmer 1993, and references therein). The radial orbit instability is thought to act efficiently during collisionless collapse and is then argued to be the leading mechanism that makes cold and spherical initial configurations evolve into generally triaxial configurations (Aguilar & Merritt 1990; Polyachenko 1992). The instability may also be responsible for a reduction of the value of the central concentration reached during collapse (Merritt & Aguilar 1985); in fact, the evolution of concentrated anisotropic systems into ellipsoids is accompanied by a drastic softening of the density distribution (Stiavelli & Sparke 1991). As is the case for many other unstable systems, evolution tends to remove the source of instability and thus, in our case, to decrease the initial excess of radial orbits.
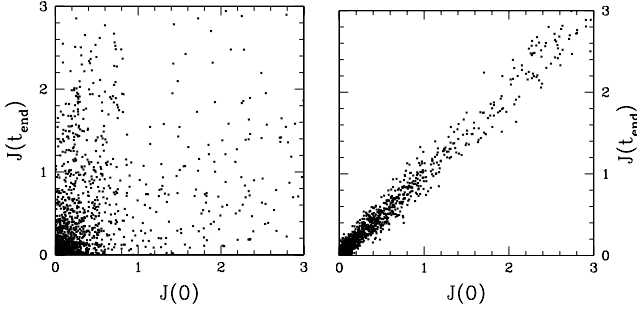
Fig. 5. Scatter plot (final vs. initial values) for the single-particle specific angular momentum. Comparison between a clumpy simulation (run $C4.2$; *left panel*) and its symmetrized version (run $S4.2$; *right panel*). Units for J are pc^2/yr, see Sect. 2.

Therefore, the threshold of instability should provide an upper limit to the global anisotropy of objects produced by collisionless collapse.

Our simulations largely confirm the general validity of this picture and the general applicability of the Polyachenko & Shukhman (1981) criterion. In particular, simulations $C2.3$ and $C2.4$ are characterized by a value of $\kappa > 1.7$ and lead to more flattened configurations than $C2.1$ and $C2.2$. Also the drop in the central concentration in simulation $C1.10$ with respect to $C1.9$ might be related to the action of the radial-orbit instability. Most of the end states are characterized by relatively high anisotropy (generally $\kappa > 1.5$, and values around 1.7 are not infrequent) and thus it seems that evolution tends to prefer a state very close to the stability boundary (as studied for the $f^{(\nu)}$ family of models in Paper I by means of an extensive set of simulations). (An interesting finding is that symmetrized initial conditions, although artificial, can lead to spherical final states still able to sustain a large number of radial orbits ($\kappa \approx 2.1$ for simulation $S4.2$)).

5.3. Angular momentum mixing

Simulations with homogeneous initial conditions generate quasi-equilibrium final configurations that not only suffer from significant mass loss, but also exhibit unusual features in their anisotropy profiles (see Sect. 7.3 and Fig. 8).

If the degree of symmetry in the initial conditions is excessive, little room is left for relaxation in the (E, J^2) phase space even if the process itself may be violent and lead to mass shedding. This is confirmed by the fact that little or no mixing is observed in the single-particle angular momentum distribution for homogeneous simulations, as reported in Fig. 5 (see also May & van Albada 1984). In fact, if the system evolves remaining close to spherical symmetry, the conservation of single particle angular momentum imposes severe constraints on the dynamical properties of the end-state of the collapse. On the other hand, a certain degree of clumpiness, even if limited to either position or velocity space, leads to angular momentum mixing. This is confirmed by two test simulations, $CV5.1$ and $CP5.2^*$, where mixing indeed turns out to be quite efficient and leads to J relaxation much like in the left panel of Fig. 5 (see also Appendix).
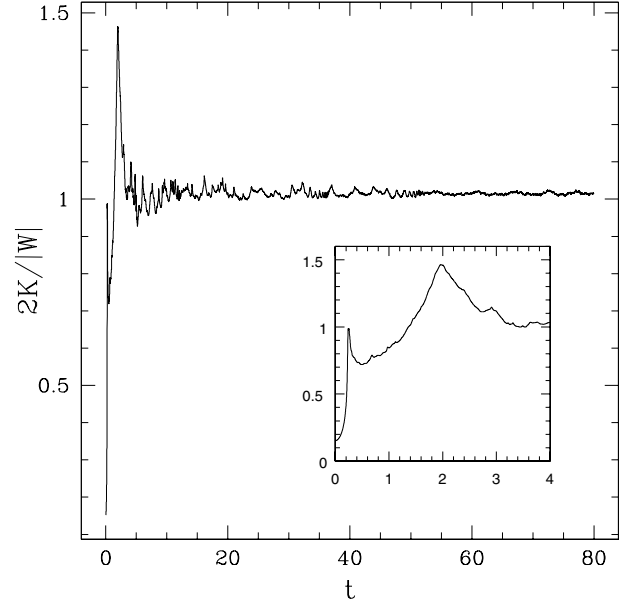

Fig. 6. Evolution of the virial ratio during run $C4.4$, characterized by the presence of many small cold clumps. The insert box zooms in on the evolution at the beginning of the simulation, when a first collapse occurs, followed by an expansion of the clumps while collapsing toward the center of mass of the system. The virial ratio in the final stages of the simulation is slightly above unity because of mass loss.

Clumps thus help the system reach a "universal" final state from a variety of initial conditions, which can explain the similarity of the density profiles observed in the final products of collapse simulations (see Sect. 7).

5.4. Dependence on the degree of clumpiness

A few simulations with a large number of clumps (400 in $C4.5$ and 80 in $C4.3$) and a spatial filling factor above unity confirm that, in the limit of large N_C, the evolution of the system approaches that of collapse simulations based on homogeneous conditions, with end-states characterized by a flat core and a low anisotropy content. A number of clumps of order 10 to 20 thus seems to be optimal for an efficient violent relaxation.

Even when limited to either position or velocity space, clumpiness can be important and still lead to end-states with general properties similar to those of the standard clumpy simulations considered in this paper (see $CV5.1$ and $CP5.2$ entries in Tables 1–2 and Sect. 7.5).

We also studied the dependence of the results of collisionless collapse on the spatial filling factor of the clumps. To do this, we took advantage of the ability of *GyrFalcON* to deal with systems with different scales and ran a simulation ($C4.4$) initialized with 80 *small* cold clumps (i.e. with a radius $R_C = 2.8$ kpc distributed in a sphere of radius 40 kpc). For this simulation, evolution basically occurs in two stages, with a first collapse in which strongly bound structures are formed in a very short time, followed by subsequent merging (see Fig. 6). Interestingly, the outcome of this simulation is highly isotropic ($\alpha \approx 0$ out to the half-mass radius) and very concentrated. We will see (Sect. 7.5) that, even in this case, the density profile

remains very well represented by $f^{(\nu)}$ models (and by the $R^{1/4}$ law). For $C4.4$, after several tens of dynamical times, there remain traces (remnants) of the more strongly bound clumps, orbiting within the smooth system.

6. Conservation of Q

We recall that the quantity Q (for a discrete system of N particles $Q = \sum_{i=1,N}(J_i/|E_i|^{3/4})^{\nu}$; see also Sect. 2) has been introduced for the description of conditions in which partial violent relaxation occurs, where it is argued that information about the initial state is basically lost, except for an approximate conservation of a third quantity (in addition to total energy and total number of particles). Therefore, it would be wrong to invert the argument and imagine that, by itself, the conservation of a quantity such as Q is equivalent to the picture of incomplete violent relaxation. In particular, we note that, judging from our set of simulations, Q is well conserved for homogeneous initial conditions, both in the velocity and position space. However, this is less relevant to our goals, since homogeneous conditions do not allow mixing and violent relaxation at the level of angular momentum space to operate properly. Therefore, it is not surprising to find that the end-products of simulations with homogeneous initial conditions tend to be less well represented by the $f^{(\nu)}$ models, in spite of their relatively good conservation of Q.

In this section we will show that the issues involved in the conjectured conservation of Q and the indications obtained from our simulations are complex. Therefore, it would be pointless to continue further in this direction, looking for a better definition of what might be defined as "acceptable degree of conservation" or searching for other quantities that might be conserved better than Q. Instead, to make a decisive test about the merits of our approach, we should take the models that have been constructed (by means of the *Ansatz* of the Q-conservation) and compare them in detail with the results of collisionless collapse obtained from our simulations. Such a test will be addressed in the following Sect. 7.

6.1. The "observed" conservation

The value of Q, computed with $\nu = 1/2$, is approximately conserved for a wide range of initial configurations. By approximate conservation we mean that $\Delta Q \leq 0.5$, although in some cases we have conservation as good as $\Delta Q \approx 0.01$. As a general rule, Q is better conserved if the initial virial ratio is not too low.

A curious property is that all clumpy simulations appear to lead to the *same* value of Q, with a scatter on the order of 10% (see Table 3). (I.e. the scatter is *less* than the mean deviation from exact conservation, around 20−30%.) This result can be interpreted, at the level of the simulations, by considering that, independently of the specific details of the initial clumpy conditions, the large scale structure of the end products of the simulations is very similar, with respect both to physical scales (constrained by the conservation of mass and energy in the collapse) and to dimensionless dynamical properties at large radii (see Sect. 7). In addition, the fact that the values of (M, E_{tot}, Q)

Table 3. Best fit $f^{(\nu)}$ models for the set of high resolution runs (series $C2$ and $C3$). The various columns give: run identifier, model identifier, mean value of the absolute relative deviations from the density of the simulations, mean value of the absolute deviations in the pressure anisotropy profile, mean value of the absolute relative deviations in the energy distribution, and final value of Q.

	$f^{(\nu)}$	$\langle|\Delta\rho/\rho|\rangle$	$\langle|\Delta\alpha|\rangle$	$\langle|\Delta E/E|\rangle$	Q
$C2.1$	(1/2; 4.8)	0.11	0.07	0.23	1.24
$C2.2$	(1/2; 4.8)	0.11	0.06	0.22	1.33
$C2.3$	(5/8; 5.0)	0.12	0.06	0.21	1.35
$C2.4$	(7/8; 5.6)	0.14	0.08	0.23	1.33
$C3.1$	(3/8; 5.6)	0.10	0.22	0.18	1.33
$C3.2$	(3/8; 5.4)	0.11	0.19	0.22	1.26
$C3.3$	(1/2; 5.2)	0.17	0.16	0.20	1.64
$C3.4$	(5/8; 5.4)	0.12	0.05	0.18	1.40
$C3.5$	(1/2; 6.2)	0.09	0.20	0.15	1.35
$C3.6$	(3/8; 5.2)	0.13	0.05	0.20	1.35

realized at the end of the simulations are approximately constant is consistent with the fact that the best-fit models do not exhibit wide variations in the values of Ψ and ν (cf. Table 3 and the discussion of parameter space given by Bertin & Trenti 2003, Sect. 3).

Strict conservation is not meaningful, for a number of reasons. Indeed, during collisionless collapse even the total number of particles N and the total energy E_{tot} are not conserved, if we refer these quantities to the final set of *bound particles*; it was noted (Stiavelli & Bertin 1987) that the non-conservation of Q actually correlates with the non-conservation of N and E_{tot}. A simple argument also warns us that the conservation of Q should not be meant to apply to all conditions. The reason is that, if we refer to the proposed definition, Q cannot be conserved in the limit of an infinitely cold collapse. In fact, for an infinitely cold collapse (i.e. for $u \to 0$, with the stars kept at fixed initial positions), at the beginning of the simulation we would have $Q \to 0$ (because the single-particle angular momenta vanish, in the limit of vanishing initial velocities, while the single-particle binding energies remain at a finite value). On the other hand, at the end of the simulation, the formation of a quasi-isotropic core with finite kinetic energy content requires that the final value of Q be finite.

Furthermore, the quantity Q is referred to an ideal case characterized by spherical symmetry, while, as noted earlier, both the initial and the final configurations in our simulations of collisionless collapse can exhibit significant deviations from spherical symmetry. To get an estimate of changes of Q associated with deviations from spherical symmetry, we have considered a (1/2; 3) $f^{(\nu)}$ model, unstable against the radial orbit instability (Paper I), and let it evolve; the final quasi-equilibrium state is characterized by $\epsilon \approx \eta \approx 0.73$ and is associated with a change $\Delta Q = 0.12$. Similar changes are observed by stretching artificially an $f^{(\nu)}$ model to a non-spherical geometry, with $\epsilon = 1$ and $\eta \approx 0.7$. But these changes are given for comparison only, since they are not related to conditions in which violent relaxation takes place.
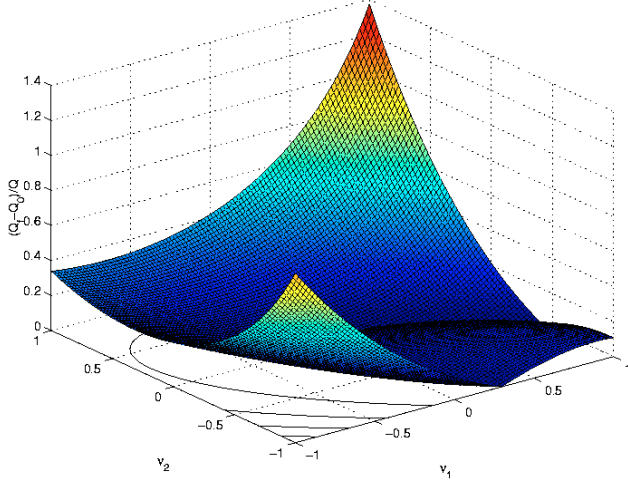
Fig. 7. Conservation of the general functional $\tilde{Q}$ (see Eq. (1)) in a typical simulation ($C4.1$).

6.2. General polynomial dependence

Although aware of the fact that we should not really look for quantities conserved exactly during collisionless collapse, we decided to test the paradigm of Q conservation further by considering the more general class of Q functionals, defined, for a system of N points, as:

$$\tilde{Q} = \sum_{i=1}^{N} \frac{J_i^{\nu_2}}{|E_i|^{\frac{3}{4}\nu_1}}, \tag{1}$$

where ν_1 and ν_2 are free parameters. We explored the parameter space $-1 \leq \nu_1 \leq 1$ and $-1 \leq \nu_2 \leq 1$. The functional Q used to construct the $f^{(\nu)}$ models corresponds to the condition $\nu = \nu_1 = \nu_2 > 0$, which guarantees the desired asymptotic behavior for the associated density $\rho \sim r^{-4}$ at large radii.

We studied the change in the value of this functional computed at the beginning and at the end of a typical simulation (10^5 particles in 10 cold clumps, run $C4.1$; see Fig. 7). If we focus on the $\nu_1 = \nu_2 = \nu$ condition, the best conservation would be attained for low values of ν.

7. Fit with the $f^{(\nu)}$ models

We first fit the density and the pressure anisotropy profiles, $\rho(r)$ and $\alpha(r)$, of the end-products of our simulations by means of the $f^{(\nu)}$ family of models. The phase space properties of the best-fit model thus identified are then compared with those of the end-products of the simulations.

Smooth, angle-averaged simulation profiles are obtained by binning the particles in spherical shells and averaging over time, based on a total of 20 snapshots taken from $t = 64$ to $t = 80$, at an epoch when the system has already settled down in a quasi-equilibrium configuration. For the $f^{(\nu)}$ models, the parameter space explored is that of an equally spaced grid in (ν, Ψ), with a subdivision of $1/8$ in ν, from $3/8$ to 1, and of 0.2 in Ψ, from 0.2 to 14.0 (corresponding to the grid of models studied in Paper I). The mass and the half-mass radius of the models are fixed by the scales set by the simulations.

A minimum-χ^2 analysis is then performed, with error bars estimated from the variance in the time average process used to obtain the smooth simulation profiles. A critical step in this fitting procedure is the choice of the relative weights for the density and the pressure anisotropy profiles. We adopted equal weights for the two terms, checking a posteriori that their contributions to χ^2 are of the same order of magnitude.

7.1. Density profiles

Since the half-mass radius r_M and the total mass M are kept fixed in the fitting procedure, we are left with two degrees of freedom (i.e., the dimensionless parameters ν and Ψ). In practice, given the general behavior of the density profile of the $f^{(\nu)}$ models (see Fig. 3 in Paper I), at large radii the freedom in the fit is limited. Therefore, the excellent match at large radii to the density profile of the end-products of the simulations demonstrates that the $f^{(\nu)}$ family has been constructed on solid physical grounds. Different values of (ν, Ψ) correspond to different shapes of the inner potential well and of the anisotropy profile. As exemplified by Figs. 9–11, the density of the final systems produced by the high resolution set of simulations ($C2$ and $C3$) is well represented by the best-fit $f^{(\nu)}$ profile over the entire radial range, from 0.1 to 10 half mass radii. The fit is satisfactory not only in the outer parts, where the density falls by *nine orders of magnitude* with respect to the central regions, but also in the inner regions. The mean absolute relative deviation between simulations and models ($\langle|\Delta\rho/\rho|\rangle = (1/N_g) \sum_{i=1}^{N_g} |\rho_{\text{sim}}(r_i) - \rho_{\text{model}}(r_i)|/\rho_{\text{sim}}(r_i)$), computed over this extended radial range, is usually around 10% (see Table 3); here N_g represents the number of radial grid points.

With a similar procedure, we have studied the end-products of simulations characterized by different numbers of particles and clumps ($C1$ and $C4$). No significant changes in the quality of the fits are found if we focus on simulations characterized by clumpy initial conditions (with the possible exception of those run with $N_C \geq 80$).

7.2. Projected density profiles

The end-products of collisionless collapse are known to be characterized by projected density profiles generally well fitted by the $R^{1/4}$ law (de Vaucouleurs 1948), provided that the collapse factor is large (i.e., that the initial virial ratio u is small; see van Albada 1982; Londrillo et al. 1991). With our set of simulations we confirm this result and we extend it by means of the $f^{(\nu)}$ models.

The successful comparison between models and simulations is interesting because, depending on the value of u, some simulations lead to configurations that exhibit deviations from the $R^{1/4}$ law. In these cases, the density profile projected along the line of sight is characterized by an $R^{1/n}$ behavior with $n \neq 4$. For example, the $C2.4$ simulation, which starts with a low collapse factor, has a best fit index $n \approx 3$, while the the simulation $C3.1$, which has a large collapse factor, is best represented by a profile with $n \approx 5$. Yet these systems all turn out to be well
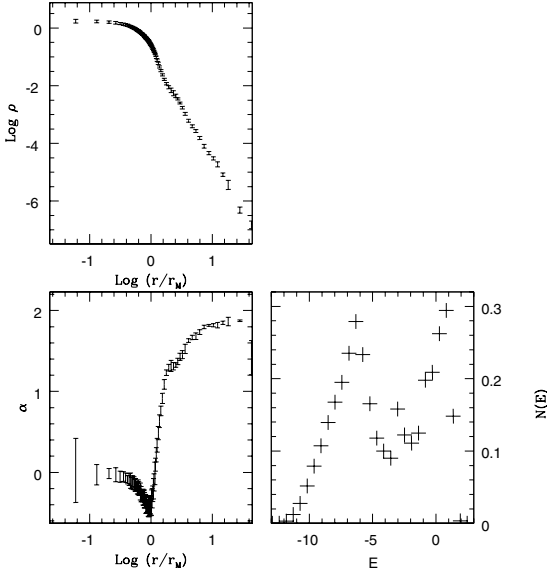
Fig. 8. Density and anisotropy profiles (*left frames*) and energy density distribution (*right frame*) for simulation *U*6.2, starting from a homogeneous sphere. Note that in the vicinity of the half-mass radius the pressure anisotropy is *tangentially* biased.

Fig. 9. Comparison between the *C*3.5 simulation and the best-fit $f^{(\nu)}$ model (1/2; 6.2). The top left panel represents the density as measured from the simulation (error bars) and the best-fit profile (line). The top right panel gives the residuals from the fit. At the bottom left, the anisotropy profile of the simulation (error bars) is compared with the best-fit profile (line); the bottom right frame illustrates the energy density distribution $N(E)$. The density ρ and the single-particle energy E are given in code units.

fitted by the $f^{(\nu)}$ models. Therefore, the family of models that we have identified might also be useful for describing systematic structural changes in galaxies, in the framework of the proposed weak homology of elliptical galaxies (Bertin et al. 2002).

7.3. Pressure anisotropy profiles

In our simulations the pressure anisotropy profiles follow the general trend expected for the process of collisionless collapse. In particular, the final configurations are characterized by an isotropic core, with $\alpha \approx 0$, while the outer regions have a strongly radially biased anisotropy (up to $\alpha = 2$). The transition region ($\alpha \approx 1$) is located around the half-mass radius (see column r_α/r_M in Table 2). Higher values of $2K_r/K_T$ are associated with lower values of r_α/r_M. For clumpy initial conditions (with the possible exception of those run with $N_C \geq 80$), the anisotropy profile $\alpha(r)$ is a monotonic increasing function of the radius. A curious feature is found for the results of collapse of uniform spheres (runs *U*). Here (see Fig. 8) the core is basically isotropic, with the region around the half-mass radius exhibiting an excess of *tangential* orbits (up to $\alpha \approx -0.4$). In the outer parts, but with a very sharp transition, the pressure profile becomes radially biased. In correspondence to the dip in α, where $\alpha < 0$, we note a clear feature in the density profile (see Fig. 8). Uniform spheres initialized with a very small particle number ($N < 10^4$) do not show this behavior; for them the pressure anisotropy rises quite regularly, although the profile is significantly affected by Poisson noise.

In conclusion, for all the clumpy *C* runs (again, we should mention, with the possible exception of those runs with $N_C \geq 80$), the anisotropy profile is represented extremely well by our models, with a mean absolute error
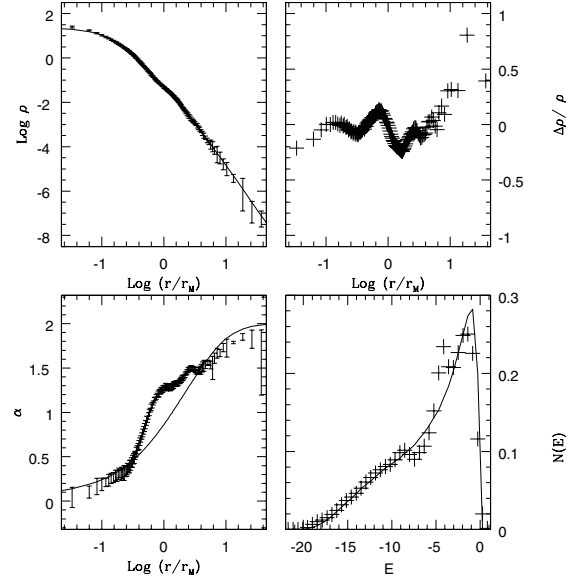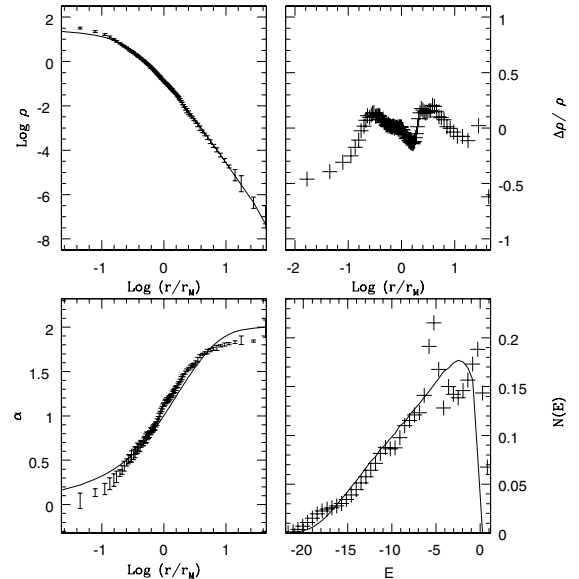

Fig. 10. Comparison between the *C*2.1 simulation and the best-fit $f^{(\nu)}$ model (1/2; 4.8), shown as in Fig. 9.

$(\langle|\Delta\alpha|\rangle = (1/N_g) \sum_{i=1}^{N_g} |\alpha_{\text{sim}}(r_i) - \alpha_{\text{model}}(r_i)|)$ typically around 0.1 but often as low as 0.05 (see Table 3).

To some extent, the final anisotropy profiles for clumpy initial conditions are found to be sensitive to the detailed choice of initialization. In other words, runs starting from initial conditions with the same parameters, but with a different seed in the random number generator, give rise to slightly different profiles. In any case, the agreement between the simulation and the model profiles remains very good (see Figs. 9–11).
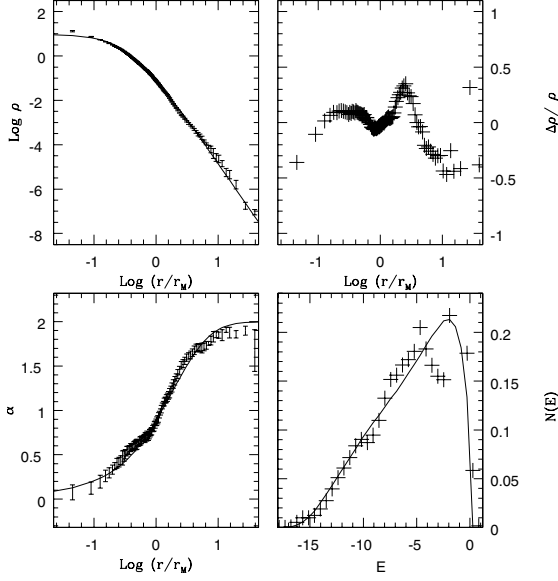
Fig. 11. Comparison between the $C3.4$ simulation and the best-fit $f^{(v)}$ model (5/8; 5.4), shown as in Fig. 9.

7.4. Comparison at the level of phase space

At the level of phase space, we have performed two types of comparison, one involving the energy density distribution $N(E)$ and the other based on $N(E, J^2)$. The chosen normalization factors are such that:

$$M = \int N(E)\mathrm{d}E = \int N(E, J^2)\mathrm{d}E\mathrm{d}J^2. \tag{2}$$

The energy distributions $N(E)$ that we find (see Fig. 9–11), qualitatively similar to those obtained in earlier investigations (see Fig. 2 in van Albada 1982 and Fig. 10 in Udry 1993), are characterized by an approximate exponential behavior at low energies ($N(E) \propto \exp(-aE)$) with a rapid cut-off near the origin, which is argued to go as $|E|^{5/2}$ because the potential is Keplerian in the outer parts (Udry 1993; see also the discussion by Jaffe 1987; and by Bertin & Stiavelli 1989). The final states of the simulations also show the presence of particles with positive energy, escaped from the system.

In Fig. 9 (bottom right frame) we plot the final energy density distribution for the simulation run $C3.5$ with respect to the predictions of the best-fit model identified from the study of the density and pressure anisotropy distributions. Similar plots are given in the following figures for other simulations. The agreement is very good ($\langle|\Delta E|\rangle \approx 0.2$, see Table 3), especially for the strongly bound particles. In particular, this means that we are correctly describing the innermost part of the system. The energy distribution for less bound particles (i.e. those associated mostly with the outer parts of the system) is less regular and sometimes presents a double peak (e.g., see Fig. 10), which obviously cannot be matched in detail by our models. This is an interesting example of the way some memory of the initial state can be preserved (the extra-peak is indeed related to the initial distribution of binding energies) and a direct sign of the incompleteness of violent relaxation.

Finally, at the deeper level of $N(E, J^2)$, simulations and models also agree rather well, as illustrated in the four panels
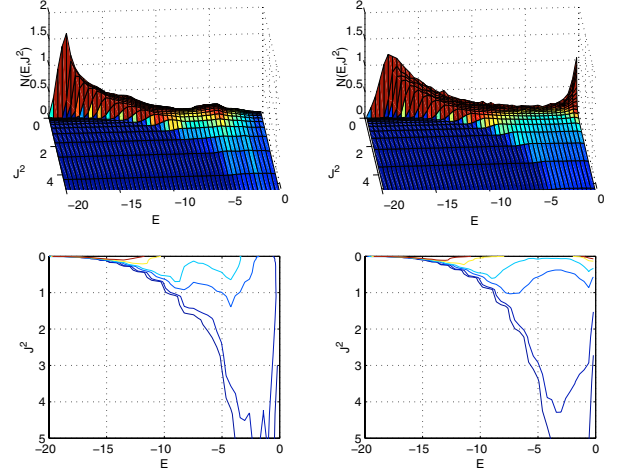

Fig. 12. Final phase space density $N(E, J^2)$ (*left column*) for the simulation $C3.5$, compared with that of the best fitting (1/2; 6.2) $f^{(v)}$ model (*right column*).
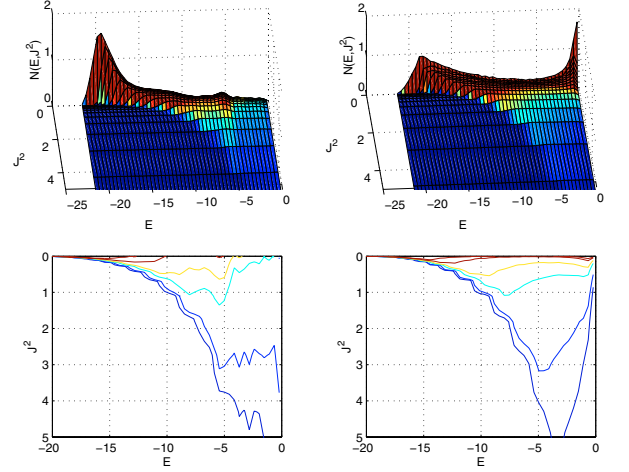

Fig. 13. Final phase space density $N(E, J^2)$ (*left column*) for the simulation $C2.1$, compared with that of the best fitting (1/2; 4.8) $f^{(v)}$ model (*right column*).

of Figs. 12–14. For the cases shown, the distribution contour lines are in good agreement in the range from $E_{\min}$ to $E \approx -4$; however, the theoretical models show a peak located near the origin, not present in the simulations, which is related to the Jacobian factor arising from the transformation of the $f^{(v)}$ distribution function from the $(\boldsymbol{x}, \boldsymbol{w})$ to the (E, J^2) space.

7.5. An additional test to characterize clumpy initial conditions

As an additional test to characterize the detailed effects of clumpiness, we studied the end-products of the $CV5.1$ and $CP5.2^*$ simulations, by comparing them with the $f^{(v)}$ models.

Although these two runs start from initial conditions rather different from our standard choice (cf. $C1$–$C3$), being homogeneous either in position ($CV5.1$) or in velocity ($CP5.2^*$) space, we note that they can be fitted very well by our family of models: (3/4; 5.4) for $CV5.1$ and (1; 6.2) for $CP5.2^*$ (with $\langle|\Delta\rho/\rho|\rangle \approx 0.1$). The good match at the level of the anisotropy
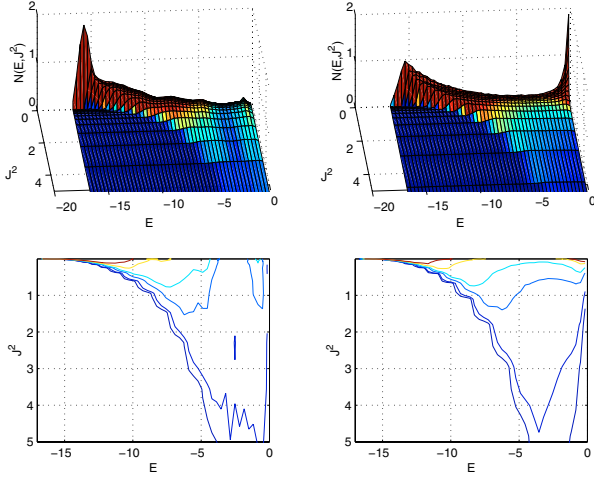
Fig. 14. Final phase space density $N(E, J^2)$ (*left column*) for the simulation $C3.4$, compared with that of the best fitting $(5/8; 5.4)$ $f^{(\nu)}$ model (*right column*).

Fig. 15. Density profile (*left*), fitted using Eq. (3) with $\gamma = 0.11$, and anisotropy profile (*right*), fitted with Eq. (4), for the simulation $C3.4$. Compare to the fit with the $(5/8; 5.4)$ $f^{(\nu)}$ model in Fig. 11.

profile $\alpha(r)$ and of the single-particle energy distribution also confirms, as discussed in the Appendix, that the requirement of clumpiness in phase space is a well posed characterization of the initial conditions. The two runs have the following behavior with respect to the Q-conservation: $\Delta Q = 0.02$ and final value $Q = 1.40$ for $CV5.1$; $\Delta Q = 0.01$ and final value $Q = 1.26$ for $CP5.2^*$.

In passing, we note that the $C4.4^*$ simulation, characterized by very small clumps, leads to a concentrated final density profile that is well reproduced by the $(1; 9.2)$ $f^{(\nu)}$ model (with $\langle |\Delta\rho/\rho| \rangle \approx 0.15$).

7.6. Separate fits to density and anisotropy profiles by means of simple analytic functions

Simple analytic descriptions of density profiles and, separately, of anisotropy profiles are often used in stellar dynamics, without a specific physical scenario of galaxy formation. For the density profile we may refer to:

$$\rho(r) = \frac{(3 - \gamma)M}{4\pi} \frac{r_0}{r^\gamma (r + r_0)^{4-\gamma}}, \tag{3}$$

where $0 \leq \gamma < 3$ is a free parameter, and M and r_0 are a mass and length scale respectively (Dehnen 1993). As discussed in Paper I, it is no surprise to find that the case $\gamma = 2$ (Jaffe 1983) captures the general properties of the density profile obtained by the simulations at the 20% level. Curiously, when we fit the density distribution of some simulations by means of Eq. (3), the best fitting index γ is very low, $\gamma \approx 0.1$ (see Fig. 15).

Similarly, for the anisotropy profile one might resort to the analytic distribution

$$\alpha(r) = 2 \frac{r^2}{r^2 + r_\alpha^2}, \tag{4}$$

with r_α being a free scale (Merritt 1985). As shown in Fig. 15, the typical shape of the anisotropy profile reached at the end of the simulations is different.
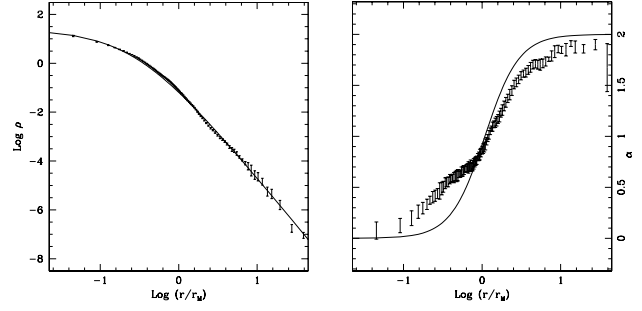
8. Discussion and conclusions

In this paper we have concentrated on nearly spherical, one-component stellar systems. As is well known, in spite of these restrictions, the equations of stellar dynamics allow almost complete freedom in the construction of self-consistent dynamical models, with the only requirement that they should be supported by a positive definite (but otherwise arbitrary) function of E and J, as a distribution function in phase space. Therefore, the full range of self-consistent one-component spherical stellar dynamical models is enormous. Most likely, the majority of these models have little to do with the systems that have been realized in nature. The main idea at the basis of the present paper is to combine clues from N-body simulations and from statistical arguments so as to pinpoint, among the enormous variety of in principle acceptable dynamical models, those few that, because of their physical justification, have a chance of matching the properties of interesting classes of numerical simulations and of observed stellar systems.

Some interesting clues had been noted earlier. With the aim of summarizing the main properties of incomplete violent relaxation during collisionless collapse, it was discovered (Stiavelli & Bertin 1987) that, by arguing that a third quantity Q (in addition to total energy and number of stars) should be included among the relevant constraints in the extremization of the Boltzmann entropy, the most probable and thus physically justified distribution function $f^{(\nu)}$ leads to models that are in *general qualitative* correspondence with the products of collisionless collapse found in numerical simulations and with the observed luminosity profiles of bright elliptical galaxies.

In the present paper we have demonstrated that the $f^{(\nu)}$ models are able to match in *surprising quantitative detail* the results of our numerical simulations. At the same time, the $f^{(\nu)}$ models exhibit projected density profiles that are well represented by the $R^{1/n}$ law (generally with $n \approx 4$; the residuals from the fit are within 0.1 magnitudes in a radial range of from 0.1 to 10 effective radii; see also Paper I). Therefore, we have demonstrated that the $f^{(\nu)}$ models, as well as the end products of the collapse simulations, are relevant to the description of the stellar distribution of elliptical galaxies. This correspondence is even more remarkable if we recall that, from the results established in the last decades, dark matter should play a dominant role in the structure of galaxies, while our approach neglects,

so far, some important ingredients among which is the presence of a massive, possibly diffuse dark halo.

Independently of stellar dynamical modeling, our simulations have shown that clumpy initial configurations allow an efficient re-distribution of the angular momenta of the individual particles during collapse: such efficient phase space mixing is precisely the main condition required for a successful application of the statistical arguments that lead to the construction of the $f^{(\nu)}$ family of distribution functions. In the past (e.g., see van Albada 1982; May & van Albada 1984; Merritt & Aguilar 1985; Londrillo et al. 1991) it has been noted that cold collapses, within a wide range of initial density profiles, generate quasi-equilibrium systems with approximate $R^{1/4}$ profiles. Here we confirm that the best match to approximate $R^{1/4}$ profiles is obtained from initiallly clumpy configurations. It thus appears that collapses starting from artificially uniform and spherically symmetric initial conditions retain too much memory of the initial conditions and are unable to evolve into a universal density distribution. Therefore, it is interesting to find that precisely those initial conditions that look more plausible and realistic from the physical point of view lead to end products able to match the stellar distribution of observed systems in detail. We may then conclude that collisionless collapse from clumpy initial conditions followed by violent relaxation is indeed a formation mechanism relevant to elliptical galaxies.

If we now take the point of view of stellar dynamical modeling and examine the foundation of the $f^{(\nu)}$ family of models, we note that many collapse simulations show Q-conservation at the 20% level or better (e.g., $C1.1$, $C2.1$ and $C3.4$). But it is even more surprising to find that the end products can be fitted so well by the $f^{(\nu)}$ models. Such good fits make it clear that the assumption of Q conservation narrows down the very wide range of self-consistent dynamical models to precisely those few systems whose properties match both observed systems and the end products of collisionless collapse. One must conclude that the value of the Q-conservation assumption goes beyond mere "physical plausibility" and "mathematical convenience": it does serve as a sound physical basis for the construction of dynamical models of partially relaxed stellar systems.

We should emphasize that such detailed *quantitative* correspondence with observed systems and with the end products of collisionless collapse comes as a complete surprise, because the two parameters that can be varied within the $f^{(\nu)}$ family of models (i.e., ν and Ψ) leave very little freedom with respect to density and anisotropy profiles (see Paper I). Especially noteworthy are not only the match of the density profile over nine orders of magnitude but also the excellent agreement of the velocity anisotropy profiles between the $f^{(\nu)}$ models and several end products of collapse from clumpy initial conditions (see Figs. 9–11 and Table 3).

Yet one cannot claim that the $f^{(\nu)}$ models give a fully satisfactory description of the phase space structure of systems produced via incomplete violent relaxation. In fact, the associated $N(E, J^2)$ distribution is characterized by singular behavior near the origin in the (E, J^2) plane, which is not present in the end-states of the simulations. In spite of this discrepancy between models and end-products of the simulations, the integrated properties (e.g., $N(E)$, $\alpha(r)$ and $\rho(r)$) are very well

reproduced. This confirms the fact that a variety of different distributions in phase space can lead to the same integrated properties. In this respect it appears that, if we refer to the extreme outer parts of the system (with $r \gg r_{\mathrm{M}}$, and $E \rightarrow 0$) the previously studied f_∞ models (Bertin & Stiavelli 1984), with their regular distribution function $f(E, J^2) \approx |E|^{3/2}$ at low values of $|E|$, might still have an advantage over the $f^{(\nu)}$ models.

Another interesting (although partly known) result of the present paper is that the velocity distributions of the end products of the collapse simulations and of the best fitting models possess, in many cases, a rather strong radial anisotropy. In some of the collapse simulations we see clear signs that the radial-orbit instability has been active (as indicated by the correlation between final ellipticity η and anisotropy content $2K_r/K_T$; cf. Fig. 4), resulting in end products that are close to the threshold for the onset of the radial-orbit instability. In general, systems that are unstable with respect to the radial-orbit instability should evolve into marginally stable systems (see also the study of the unstable $(1; 3.2)$ $f^{(\nu)}$ model in Paper I). In view of the good correspondence between the results of the formation processes studied in this paper and important observed properties of elliptical galaxies, we may argue that ellipticals are also likely to lie close to the threshold of radial-orbit instability. This would happen if elliptical galaxies, during their formation process, indeed went through a collisionless phase characterized by strong radial motions (such as collapse or head-on mergers). We plan to better quantify this connection by extending the study to two-component models and collapses, also starting from a power spectrum of perturbations representative of cosmological initial conditions.

The last remark brings us naturally to one final comment. We recall that, since collisionless dynamics is scale-free, the results obtained here can also be interpreted as relevant to the description of the collapse of dark matter halos. Clearly, since we do not include the effects related to the general Hubble expansion and we do not initialize our clumpy conditions in terms of the power spectrum of perturbations appropriate for a given cosmological epoch, a direct comparison between our set of numerical experiments and the profiles of dark matter halos obtained in ΛCDM simulations (Navarro et al. 1997; Moore et al. 1998) would not be justified. Still, our experiments can be considered as one example of final equilibrium realizations of a dark halo, when initial conditions are varied outside the prescriptions consistent with the currently accepted cosmological framework (see also Lemson 1995). If we now go back to our interpretation in terms of the $f^{(\nu)}$ models, it is noteworthy to point out that, although the density profile of the $f^{(\nu)}$ models falls off as $1/r^4$ at large radii, in the inner parts that might correspond to the regions inside the virial radius (for a definition see Navarro et al. 1997), the density goes approximately as $1/r^{3.2}$ (see Sect. 3.1 in Paper I), which is very close to the reported $1/r^3$ value for cosmological simulations (Navarro et al. 1997; Moore et al. 1998). Since the outskirts of dark matter halos are "still collapsing", and thus their dynamical conditions are different from those under which we derived the $f^{(\nu)}$ models, this agreement appears surprisingly good and suggests further investigations.

Appendix A: A quantitative measure of clumpiness

In order to characterize the degree of clumpiness present in the initial conditions of our simulations, we may consider, in the 6-dimensional phase space, the ratio $cl = \langle \rho_{local}^{(6)} \rangle / \langle \rho^{(6)} \rangle$ of the mean local density around particles to the mean density.

We estimate the mean 6-dimensional density in phase space $\langle \rho^{(6)} \rangle$ by dividing the number of particles N by the typical total volume occupied. Since the large-scale structure in phase space is that of a sphere both in position and velocity space separately, we compute the total volume as the product of these two volumes. Each volume is calculated by assuming that the radius of each sphere is equal to the mean distance between two randomly chosen particles in the relevant space (position and velocity respectively); for example, for a homogeneous density distribution inside a sphere of unit radius, the radius determined from the adopted procedure would be ≈ 1.03.

The local density $\rho_{local}^{(6)}$ (required for calculating the average used in the definition of cl) is computed by considering one particle and by counting the number of neighboring particles N_{local} within a six-dimensional small sphere of fixed radius r_s (and thus by assuming an equally weighted norm in the phase space for positions and velocities). The scale r_s is chosen in such a way that, on average, a small fixed fraction of the total number of particles is enclosed. We set this fraction to be $\xi = \langle N_{local} \rangle / N \approx 1/250$. This choice ensures that we have, on average, a high filling factor within the small sphere, so that the effects of biases in the local density estimation arising from the coincidence of the center of the local sphere with the coordinates of a particle are unimportant (for a discussion on the construction of unbiased estimators for the local density, see also Casertano & Hut 1985).

The adopted scale r_s also acts as a cut-off scale to the clumpiness estimator cl, which is obviously insensitive to fluctuations at scales smaller than r_s. The dependence of the clumpiness estimator on ξ is illustrated in Fig. A.1. Eventually, diagnostic tools such as $cl(\xi)$, as a measure of the initial spectrum of inhomogeneities in phase space, will help us establish a bridge toward initial conditions representative of the cosmological context (see also comments at the end of Sect. 4.1).

For our homogeneous initial conditions (simulations of type U) the value of the clumpiness estimator is $0.65 \lesssim cl \lesssim 1$, depending on the scale considered ($cl = 0.72$ for $\xi = 1/250$). Note that the value of cl can fall below unity, because of boundary effects. In contrast, for the cold clumpy initial conditions of type $C1$, $C2$, and $C3$ (with 10 and 20 clumps, and spatial filling factor $N_C \times R_C^3/R^3 \approx 1.25$), at $\xi = 1/250$ cl takes on values above 30, with typical values around 50 and peaks up to 100. For simulation $C4.4$ (with "small" clumps, and spatial filling factor $N_C \times R_C^3/R^3 = 0.027$), cl increases to 300. Conversely, cl decreases if the number of clumps is increased (down to $cl = 15$
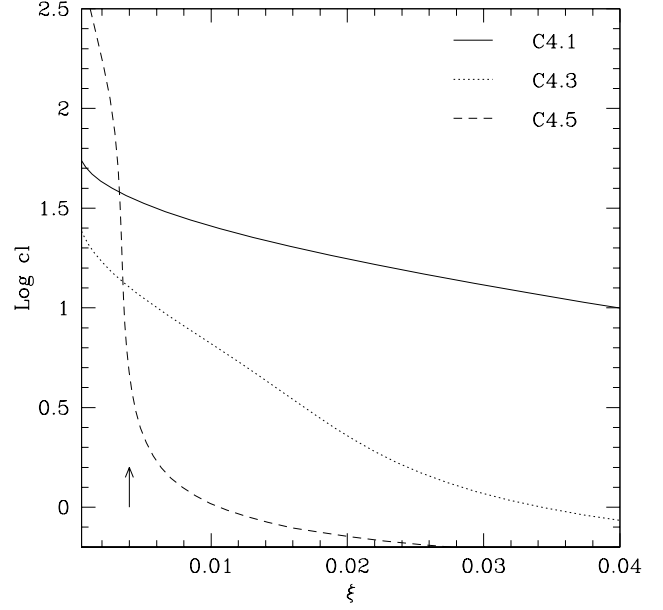

Fig. A.1. Clumpiness estimator cl as a function of $\xi = \langle N_{local} \rangle / N$, for the initial conditions of simulations $C4.1$ (10 clumps), $C4.3$ (80 clumps), and $C4.5$ (400 clumps). The spatial filling factor is kept approximately constant ($N_C \times R_C^3/R^3 = 1.1-1.3$). The arrow indicates the scale $\xi = 1/250$ to which we refer most of our estimates.
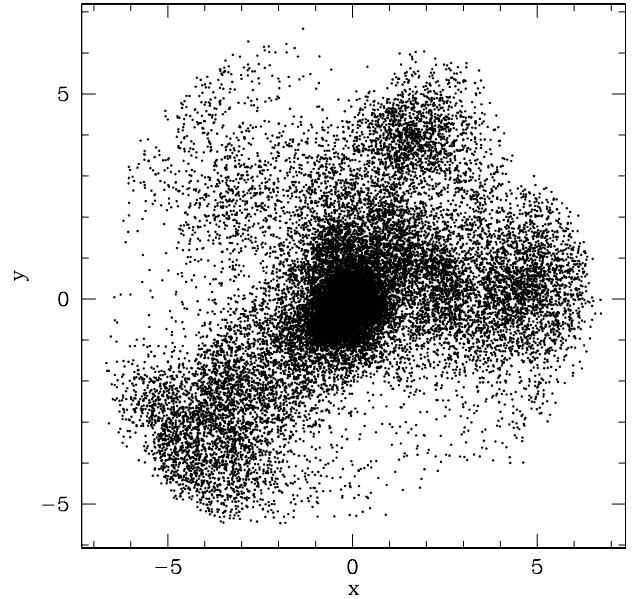

Fig. A.2. Spatial configuration at time $t = 4$ (i.e., after a few dynamical times, in the post-collapse phase) for the simulation $CV5.1$. Note the presence of clumps in position space.

for simulation $C4.3$ with 80 clumps and to $cl \approx 4.5$ for simulation $C4.5$ with 400 clumps).

With the numbers quoted above, we see that, at fixed numbers of particles, the clumpiness estimator cl varies with the number of clumps N_C used.

A.1. Clumpiness and mixing

As already anticipated in Sects. 5.3 and 5.4, for an efficient angular momentum mixing it is sufficient that clumpiness be present either in position or in velocity space. In fact, a simulation starting from uniform conditions in terms of positions but with clumpy structure in velocity space is bound to develop, after a few dynamical times, a significant clumpiness in position space (see Fig. A.2), so that the single-particle angular momenta are well mixed at the end of the simulation (much as in the left panel of Fig. 5). This result confirms that our choice for quantifying the clumpiness of a given configuration by looking at the six-dimensional phase space is indeed reasonable.

References

Aguilar, L. A., & Merritt, D. 1990, ApJ, 354, 33
Barnes, J., & Hut, P. 1986, Nature, 324, 446
Bertin, G., Ciotti, L., & Del Principe, M. 2002, A&A, 386, 149
Bertin, G., & Stiavelli, M. 1984, A&A, 137, 26
Bertin, G., & Stiavelli, M. 1989, ApJ, 338, 723
Bertin, G., & Stiavelli, M. 1993, Rep. Progr. Phys., 56, 493
Bertin, G., & Trenti, M. 2003, ApJ, 584, 729
Boily, C. M., Athanassoula, E., & Kroupa, P. 2002, MNRAS, 332, 971
Casertano, S., & Hut, P. 1985, ApJ, 298, 80
de Vaucouleurs, G. 1948, Ann. Astrophys., 11, 247
Dehnen, W. 1993, MNRAS, 265, 250
Dehnen, W. 2000, ApJ, 536, L39
Dehnen, W. 2002, J. Comp. Phys., 179, 27
Heggie, D. C., & Mathieu, R. D. 1986, Lecture Notes in Physics, The Use of Supercomputers in Stellar Dynamics, 267, 233
Hernquist, L., & Ostriker, J. P. 1992, ApJ, 386, 375
Jaffe, W. 1983, MNRAS, 202, 995
Jaffe, W. 1987, in Structure and Dynamics of Elliptical Galaxies, ed P. T. de Zeeuw (Dordrecht, The Netherlands: Reidel), IAU Symp., 127, 511
Katz, N. 1991, ApJ, 368, 325
Lemson, G. 1995, Ph.D. Thesis, Groningen University
Londrillo, P., Messina, A., & Stiavelli, M. 1991, MNRAS, 250, 54
Lynden-Bell, D. 1967, MNRAS, 131, 101
Lynden-Bell, D., & Wood, R. 1968, MNRAS, 138, 495
May, A., & van Albada, T. S. 1984, MNRAS, 209, 15
McGlynn, T. A. 1984, ApJ, 281, 13
Merritt, D. 1985, AJ, 90, 1027
Merritt, D., & Aguilar, L. A. 1985, MNRAS, 217, 787
Moore, B., Governato, F., Quinn, T., Stadel, J., & Lake, G. 1998, ApJ, 499, L5
Navarro, J. F., Frenk, C. S., & White, S. D. M. 1997, ApJ, 490, 493
Osipkov, L. P. 1979, Pis'ma Astronomicheskii Zhurnal, 5, 77
Palmer, P. 1993, Stability of collisionless stellar systems (Kluwer Academic Publishers)
Polyachenko, V., & Shukhman, I. 1981, Soviet Astron., 25, 533
Polyachenko, V. L. 1992, Soviet Astron., 36, 482
Roy, F., & Perez, J. 2004, MNRAS, 348, 62
Sersic, J. L. 1968, Atlas de galaxias australes (Cordoba, Argentina: Observatorio Astronomico)
Stiavelli, M., & Bertin, G. 1987, MNRAS, 229, 61
Stiavelli, M., & Sparke, L. S. 1991, ApJ, 382, 466
Teuben, P. 1995, ASP Conf. Ser., 77, 398
Trenti, M. 2005, Ph.D. Thesis, Scuola Normale Superiore, Pisa, in preparation
Trenti, M., & Bertin, G. 2005, A&A, 429, 161 (Paper I)
Udry, S. 1993, A&A, 268, 35
van Albada, T. 1982, MNRAS, 201, 939
Warren, M. S., Quinn, P. J., Salmon, J. K., & Zurek, W. H. 1992, ApJ, 399, 405